Coherent-phonon-driven intervalley scattering and Rabi oscillation in multivalley 2D materials

Supplemental Material

Chenyu Wang,[1,2,*] Xinbao Liu,[1,2,*] Qing Chen,[1,2,*]
Daqiang Chen,[1,2] Yaxian Wang,[1,†] and Sheng Meng[1,2,3,‡]

[1] *Beijing National Laboratory for Condensed Matter Physics and Institute of Physics, Chinese Academy of Sciences, Beijing 100190, China*

[2] *School of Physical Sciences, University of Chinese Academy of Sciences, Beijing 100190, China*

[3] *Songshan Lake Materials Laboratory, Dongguan, Guangdong 523808, China*

[*] These authors contributed equally.

[†] Email address: yaxianw@iphy.ac.cn

[‡] Email address: smeng@iphy.ac.cn

S1. TIME-DEPENDENT DENSITY FUNCTIONAL THEORY

The time evolution of electron wave functions is governed by the time dependent Kohn-Sham (TDKS) equations [1]:

$$i\frac{\partial}{\partial t}\psi_{i,\mathbf{k}}(\mathbf{r},t) = \left[\frac{1}{2m}(\mathbf{p}-\frac{e}{c}\mathbf{A})^2 + V(\mathbf{r},t)\right]\psi_{i,\mathbf{k}}(\mathbf{r},t), \tag{S1}$$

where velocity gauge is used and the external field appears in the kinetic term in the form of vector potential $\mathbf{A}(t)$.

The propagation of TDKS orbitals is implemented on the adiabatic basis $\phi_{n,\mathbf{k}}(\mathbf{r},t)$

$$\left|\psi_{i,\mathbf{k}}(\mathbf{r},t)\right\rangle = \sum_n c_{in\mathbf{k}}(t)\left|\phi_{n,\mathbf{k}}(\mathbf{r},t)\right\rangle, \tag{S2}$$

where i and n denote the band index, $\mathbf{k}$ refers to the reciprocal momentum index and $c_{in\mathbf{k}}(t)$ the time dependent coefficients. The adiabatic basis is calculated on the fly at each ionic step by diagonalizing the Hamiltonian:

$$H_{\mathbf{k}}(\mathbf{r},t)\left|\phi_{n,\mathbf{k}}(\mathbf{r},t)\right\rangle = \varepsilon_{n,\mathbf{k}}(t)\left|\phi_{n,\mathbf{k}}(\mathbf{r},t)\right\rangle, \tag{S3}$$

where $\varepsilon_{n,\mathbf{k}}(t)$ is the eigenvalue. Thus, the charge density can be calculated with $c_{in\mathbf{k}}(t)$ and $\phi_{n,\mathbf{k}}(\mathbf{r},t)$:

$$\begin{aligned}
\rho(\mathbf{r},t) &= \sum_{\mathbf{k}}\sum_i \left|\left\langle\psi_{i,\mathbf{k}}(\mathbf{r},t)|\psi_{i,\mathbf{k}}(\mathbf{r},t)\right\rangle\right|^2 \\
&= \sum_{\mathbf{k}}\sum_i\sum_n |c_{in\mathbf{k}}(t)|^2\left|\left\langle\phi_{n,\mathbf{k}}(\mathbf{r},t)|\phi_{n,\mathbf{k}}(\mathbf{r},t)\right\rangle\right|^2 \\
&= \sum_{\mathbf{k}}\sum_n\left[\sum_i |c_{in\mathbf{k}}(t)|^2\right]\left|\left\langle\phi_{n,\mathbf{k}}(\mathbf{r},t)|\phi_{n,\mathbf{k}}(\mathbf{r},t)\right\rangle\right|^2 \\
&= \sum_{\mathbf{k}}\sum_n q_{n,\mathbf{k}}(t)\left|\left\langle\phi_{n,\mathbf{k}}(\mathbf{r},t)|\phi_{n,\mathbf{k}}(\mathbf{r},t)\right\rangle\right|^2,
\end{aligned} \tag{S4}$$

where

$$q_{n,\mathbf{k}}(t) = \sum_i |c_{in\mathbf{k}}(t)|^2, \tag{S5}$$

is the population on the adiabatic basis.

For ions that are much heavier than electrons, their motions are treated classically on an averaged potential energy surface determined by the electronic distribution according to the Ehrenfest

theorem. The nuclear positions are updated following the Newton's second law[2]:

$$M_\alpha \frac{d^2\mathbf{R}_\alpha}{dt^2} = \sum_i \langle\psi_i|\nabla_{\mathbf{R}_\alpha}(\frac{1}{2m}(\mathbf{p} - \frac{e}{c}\mathbf{A})^2 + V(\mathbf{r},t))|\psi_i\rangle \tag{S6}$$

where M_α and $\mathbf{R}_\alpha$ are the mass and position of the αth ion. Eq. (S1) and Eq. (S6) represents the coupled electron-ion motion.

S2. COMPUTATIONAL DETAILS

Our TDDFT calculations are performed using the time-dependent *ab initio* package (TDAP-QE) as implemented in *Quantum Espresso* using plane wave basis [3–5]. In order to couple the two electron states we care about, a 2×2 supercell is constructed. The Brillouin zone is sampled by 9×9×1 Gamma-centered k mesh with an energy cutoff of 65 Ry. Ultrasoft pseudopotential (USPP) combined with adiabatic local density approximation (LDA) is used to describe interactions between electrons and ions.

The applied laser electric field $E(t)$ is described as a Gaussian-envelope function:

$$E(t) = E_0 cos(2\pi\omega t) exp\left[-\frac{(t-t_0)^2}{2\sigma^2}\right] \tag{S7}$$

where the width σ is 5 fs, and photon frequency ω is 0.42 fs^{-1}. The laser field reaches the maximum strength $E_0 = 0.073$ V/Å at time $t_0 = 20$ fs (see Fig. S1 the waveform). In Eq. (S1) velocity gauge is used where the vector and scalar potential of the field $E(t)$ are $\mathbf{A}(t) = -c\int_0^t \mathbf{E}(t')dt'$ and $\Phi = 0$.

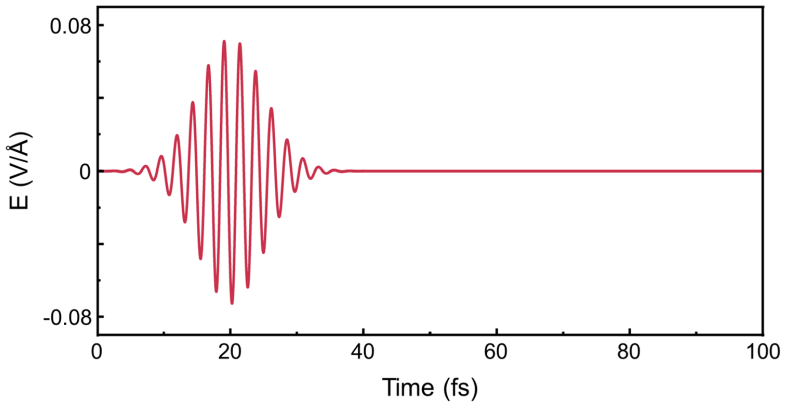

Figure S1. Waveform of the applied electric field linearly polarized along the a-axis of the crystal cell.

In the section of nonlinear phononics, we perform TDDFT-based molecular dynamics simulations using the smallest tetragonal supercell that folds the M point ($\mathbf{q} = [0.5, 0, 0]$) in the reciprocal space of the hexagonal primitive cell to the Γ point, as is shown in Figs. S2 (a) and (b). We set the starting temperature close to zero for the micro-ensemble simulation to eliminate the influence of thermal phonons and the time step to 0.1 attosecond for the electrons and 0.1 femtosecond for the ions.

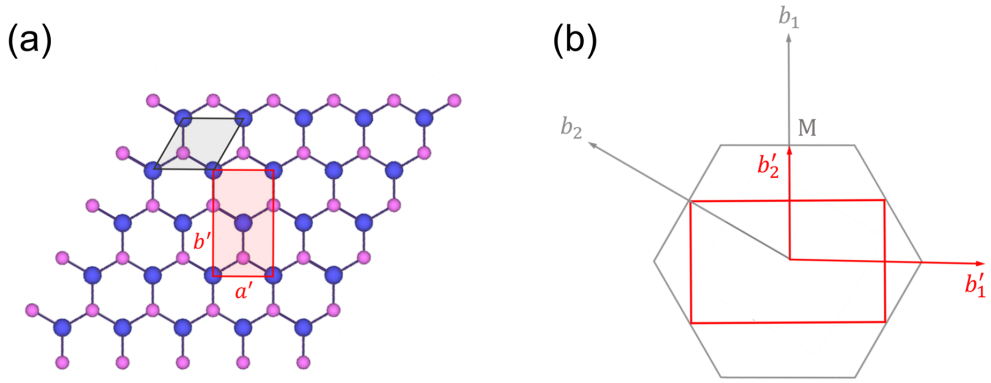

Figure S2. (a) The primitive cell (grey) and the tetragonal computational cell (red) for the molecular dynamics simulation. (b) The corresponding Brillouin zone folding from the tetragonal cell to the hexagonal cell.

S3. ELECTRON DYNAMICS UNDER THERMAL CONDITIONS

In theory, with the presence of only thermal phonons but no coherent LA(M) mode, the electron dynamics should be comparable with the experimental measurements. However, in our work, the simulated case is more or less to the other limit, i.e. large amplitude of coherent LA(M) mode but *negligible* thermal phonons. In principle, the *ab initio* simulations could reproduce the experimental condition by setting finite temperature, a large enough supercell, and simulating the process for long enough time, to guarantee a complete thermal phonon distribution. However, this

is not realistic at this point and thus beyond the scope of this work. An alternative approach to capture the thermal phonon mediated inter-valley scattering dynamics relies on the solution of the transport equation, with the electron-phonon or exciton-phonon coupling strength obtained from first-principles calculation as its input parameters [6]. There, an exponential-style decay of K valley occupation can be captured, which is similar to the experimental feature.

S4. EXCITONIC EFFECT

In principle, the excitonic effect could be fully included in the TDDFT equations, if the exact exchange-correlation (xc) potential is used [7]. In recent years, the real-time (RT) TDDFT we used in the present calculations has been demonstrated to be capable of describing the excitonic effects, using a vector potential generalized from the long-range corrected (LRC) xc kernels [8]. This approach accounts for the long-range screened electron-hole interaction and can reliably calculate the exciton formation energy and can predict optical properties with much improved consistency with various spectroscopic measurements [8].

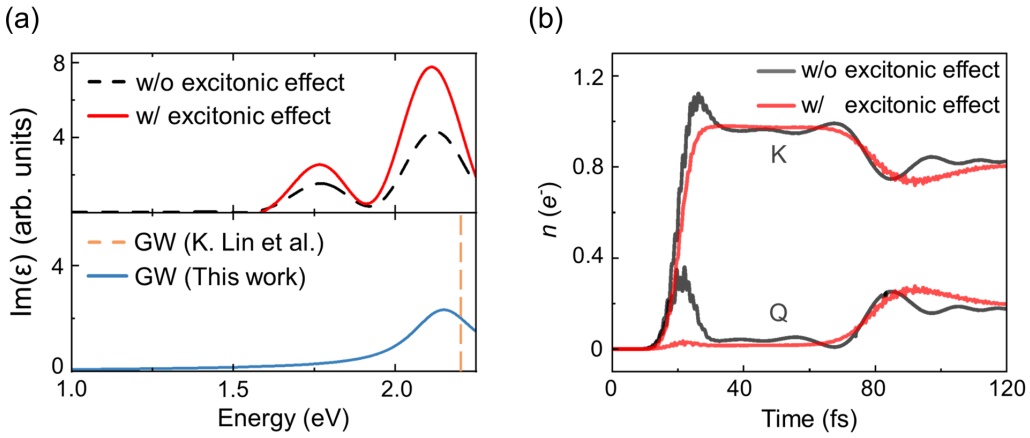

Figure S3. (a) Upper panel: Imaginary part of the dielectric function calculated within TDDFT formalism with (RT-LRC kernel, red) and without (RT-ALDA kernel, black) excitonic effect. Lower panel: Dielectric function calculated with the many body GW method (blue curve), showing the first absorption peak is at ~ 2.2 eV. The orange dashed line represents the GW band gap calculated by K. Lin *et al.* in Ref. [9]. (b) The intervalley scattering dynamics calculated with and without inclusion of the excitonic effect. We have normalized the electron occupation number to facilitate the direct comparison.

To model the excitonic effect in our simulations, we integrate such xc vector potential into our time-dependent *ab initio* package and compute the absorption spectrum of monolayer WSe_2 for a benchmark. We find in Fig. S3(a) that the inclusion of electron-hole interactions (red curve, upper panel) shifts the absorption peak down to the correct position with respect to the GW calculation [9] (blue curve, lower panel) and also results in significant enhancement in the peak intensity in comparison with the TDDFT calculation when the excitonic effects are not sufficiently included (black dashed curve, upper panel).

To estimate the excitonic effect on the coherent-phonon-mediated intervalley scattering dynamics, we simulate the temporal evolution of the photoexcited K-valley electrons with the updated xc kernel, i.e. by taking into account the long-range electron-hole interaction. We find that the LA(M) phonon mode induces a intervalley transition between the K and Q valley at $\sim$ 100 fs with the presence of electron-hole interactions, shown by the red curve in Fig. S3(b). Furthermore, the step-like scattering fashion is retained, which is the most distinguishable feature for our proposed coherent-phonon-driven mechanism. By comparing these results (red curve in Fig. S3(b)) with the original data (black curve in Fig. S3(b), the same as that in Fig. 2(b)), we conclude that the excitonic effect did not change the main message of our work.

S5. RABI OSCILLATION

In Fig. S4, we show our TDDFT simulations on the electron dynamics up to 1 ps, where the K-Q-K scattering, namely, a full Rabi oscillation cycle, is indeed observed.

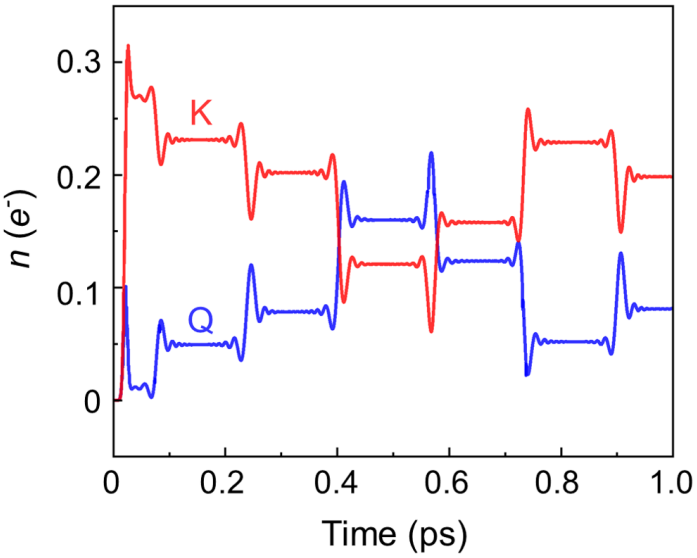

Figure S4. A full cycle of Rabi oscillation showing the K-to-Q transition and the inverted Q-to-K transition.

S6. MODE SELECTIVITY

For each mode at the M point, we carry out the same TDDFT-MD simulations as described for the LA(M) mode in the main text and extract the excited-state phonon frequency from the Fourier transform of the atomic trajectory in the photoexcited state projected onto the corresponding phonon vibrational eigenvector. Comparison of phonon frequency in ground (ω_g) and excited state (ω_e) has been listed in the following table:
where the index of the phonon mode refers to a purely energetic ordering of the phonon dispersion at M point, as shown in Fig. S5(a). The frequency of LA(M) mode (index 3) experiences a significant change compared with other modes, which indicate a strong coupling of the K state with LA(M) mode.

In Figs. S5(b) and (c), we show the corresponding electron dynamics driven by the two coherent optical modes as indicated by the colored rectangle in Fig. S5(a). While the lattice has initially been displaced to a large amplitude along their vibrational eigenmode as is done for the LA(M) mode, the electron occupation on both K and Q valley stays almost unchanged during the whole time span.

TABLE I. Ground and excited state phonon frequency

index	ω_g (THz)	ω_e (THz)
1	2.930	2.949
2	3.658	3.650
3	3.877	3.090
4	5.813	5.804
5	6.498	6.491
6	6.883	6.897
7	7.361	7.274
8	7.923	7.901
9	8.113	8.013

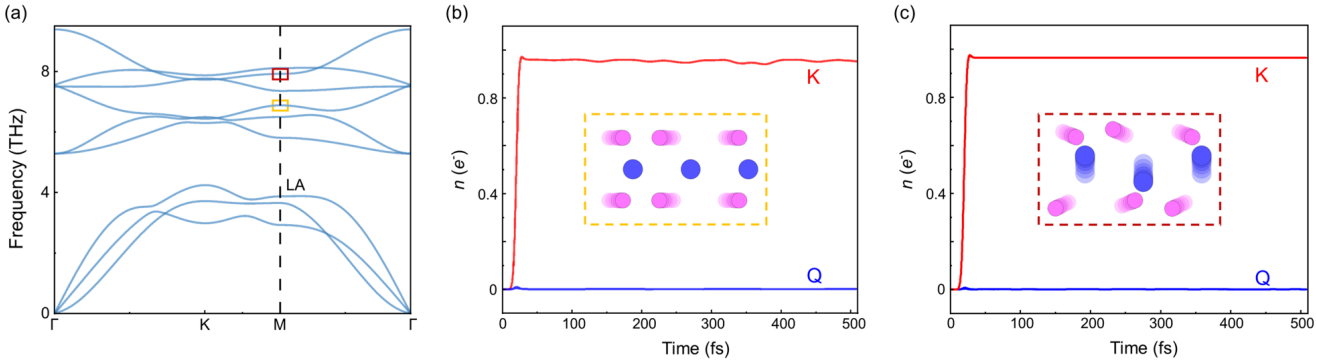

Figure S5. (a) Phonon dispersion of monolayer WSe_2. (b)-(c) Scattering calculations with different phonon modes as marked by the colored rectangle in (a). Inset illustrates their vibrational eigenmode.

S7. PERIOD OF EIGENVALUE EVOLUTION

Rewriting the time-dependent Hamiltonian as:

$$\hat{H} = \hat{H}_0 + \hat{H}_{ep}(t) \tag{S1}$$

where first term on the right-hand side refers to the unperturbed Hamiltonian and second term the electron-phonon interaction which reserves only first order expansion on atomic displacement of Coulomb interaction between electron and lattice given by the following form:

$$\hat{H}_{ep}(t) = \sum_{j,l} \boldsymbol{\mu}_l(t) \cdot V(\boldsymbol{r}_i - \boldsymbol{l}) \tag{S2}$$

Displacement of the *lth* atom should be a linear combination of all the normal mode, but herein we consider only the contribution from LA(M) mode in line with our calculation strategy:

$$\boldsymbol{\mu}_l(t) \sim \boldsymbol{e}_q e^{i(\boldsymbol{q}\cdot\boldsymbol{l}-\omega t)} \quad , \quad \boldsymbol{q} = \frac{1}{2}\boldsymbol{b}_1 \tag{S3}$$

where $\boldsymbol{q}$ denotes the wavevector of the LA(M) mode which is half the reciprocal lattice vector $\boldsymbol{b}_1$. Then we can obtain the simple property, combined with the orthogonality relation between lattice vector and its reciprocal counterpart:

$$\boldsymbol{a}_i \cdot \boldsymbol{b}_j = 2\pi\delta_{ij} \quad , \quad \boldsymbol{\mu}_l(t) = \boldsymbol{\mu}_{l+\boldsymbol{a}_i}(t + \frac{T}{2}) \tag{S4}$$

which implies that the two structures separated by half a phonon period T of LA(M) mode are actually equivalent under a translational operation, as is shown in Fig. S6.

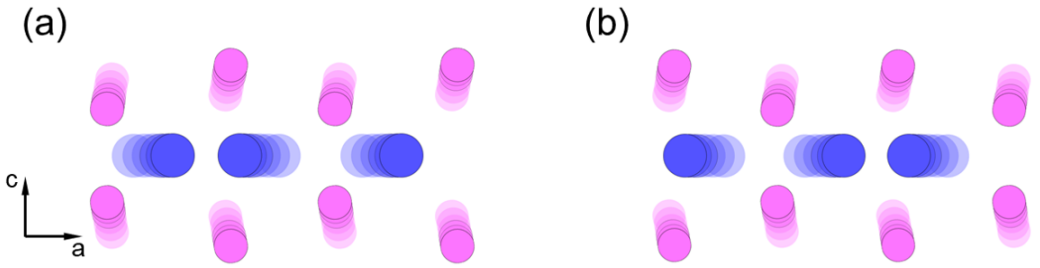

Figure S6. (a),(b) Crystal structure separated by half a phonon period.

Accordingly, we define a spatiotemporal symmetry operator for a better description of the time-periodic system:

$$\hat{X} = \hat{P}_{\boldsymbol{a}_1} \cdot \hat{\tau}_2 \tag{S5}$$

in which $\hat{P}_{\boldsymbol{a}_1}$ stands for a spatial translation by $\boldsymbol{a}_1$ and $\hat{\tau}_2$ a temporal translation by half a phonon period. From Eq. (S3) and Eq. (S4):

$$[\hat{P}^2_{\boldsymbol{a}_1},\ \hat{H}(t)] = 0 \quad , \quad [\hat{X},\ \hat{H}(t)] = 0 \tag{S6}$$

In this case, the instantaneous eigenmodes of $\hat{H}(t)$ are simultaneous eigenmodes of operator $\hat{P}_{\boldsymbol{a}_1}$ and $\hat{X}$. Also, since the two operators are unitary, their eigenvalues are roots of unity:

$$\hat{P}^2_{\boldsymbol{a}_1}|K(t)\rangle = e^{i\phi}|K(t)\rangle \tag{S7a}$$

$$\hat{X}|K(t)\rangle = e^{i\varphi}|K(t)\rangle \tag{S7b}$$

Noting that we can insert Eq. (S5) into Eq. (S7b) and then compare to Eq. (S7a):

$$\hat{P}_{\boldsymbol{a}_1}|K(t+\frac{T}{2})\rangle = e^{i\varphi}|K(t)\rangle \tag{S8a}$$

$$\hat{P}_{\boldsymbol{a}_1}|K(t)\rangle = e^{i\gamma}|K(t+\frac{t}{2})\rangle \tag{S8b}$$

Expanding the commutator in eq. (S6), one obtains:

$$\hat{P}_{\boldsymbol{a}_1}\hat{H}(t)\hat{P}^{-1}_{\boldsymbol{a}_1} = \hat{H}(t+\frac{T}{2}) \tag{S9}$$

Imposing the spatial translational operator on the eigen equation satisfied by instantaneous eigenstate $|K(t)\rangle$ and combine with Eq. (S9), we finally have:

$$\hat{H}(t+\frac{T}{2})|K(t+\frac{T}{2})\rangle = \varepsilon_K(t)|K(t+\frac{T}{2})\rangle \tag{S10}$$

Since mode $|K(t+\frac{T}{2})\rangle$ has originally been leveled as $\varepsilon_K(t+\frac{T}{2})$, the time evolution of eigenmode clearly has a period at half that of the phonon mode, that is:

$$\varepsilon_K(t) = \varepsilon_K(t+\frac{T}{2}) \tag{S11}$$

S8. Q-VALLEY OCCUPATION FOR THE MODEL SYSTEM

For our two-level Hamiltonian, we write the state of the system as a power series [10]:

$$|\psi(t)\rangle = |\psi(t)\rangle^{(0)} + |\psi(t)\rangle^{(1)} + |\psi(t)\rangle^{(R)}, \tag{S12}$$

with

$$|\psi(t)\rangle^{(0)} = e^{-\frac{i}{\hbar}\int_0^t dt'\varepsilon_K(t')}|K(t)\rangle, \tag{S13}$$

$$|\psi(t)\rangle^{(1)} = |Q(t)\rangle\int_0^t dt_1 e^{-\frac{i}{\hbar}\int_{t_1}^t dt\varepsilon_Q(t')}\langle\dot{Q}(t_1)|K(t_1)\rangle e^{-\frac{i}{\hbar}\int_0^{t_1} dt'\varepsilon_K(t')}, \tag{S14}$$

$$|\psi(t)\rangle^{(R)} = C_R(t)|K(t)\rangle, \tag{S15}$$

where $|K(t)\rangle$ and $|Q(t)\rangle$ are the real-time eigenstates of the model Hamiltonian with $\varepsilon_K(t)$ and $\varepsilon_Q(t)$ being their eigenvalues, correspondingly. We set the system to start on the $|K(0)\rangle$ state in line with the condition under optical excitation. The subsequent evolution of wavefunction of the

K state includes the usual adiabatic part (Eq. (S13)) and the residual higher order contributions (Eq. (S15)). Here we have substituted all the complex expressions for high order corrections by a single term $C_R(t)$ and the occupation number on K state is obtained according to particle conservation in our calculations. On the other hand, for population dynamics at the Q valley, we truncate the expansion to the first order as in Eq. (S14) and the occupation number could be calculated as the squared modulus of the coefficient.

S9. DEFORMATION POTENTIAL AND NONADIABATIC COUPLING MATRIX ELEMENT

The deformation potential is defined as [11, 12]:

$$\mathcal{D} = \langle Q(t)| \frac{\delta H(t)}{\delta d(t)} |K(t)\rangle \tag{S16}$$

where the variation of the Hamiltonian is taken with respect to the distortion *d(t)* along the phonon coordinate of LA(M) mode. For numerical calculation, the deformation potential is obtained using a finite difference approach:

$$\mathcal{D}^2 = \frac{(\varepsilon_K - \varepsilon)(\varepsilon_Q - \varepsilon)}{d^2} \tag{S17}$$

where ε is the K valley energy upon finite distortion d. Generally, the absolute value of deformation potential could be viewed as a constant during the lattice vibration and it is obtained from first principle by calculating the energy variation at the moment denoted by the vertical dashed line in Fig. S7(a). However, the sign is somewhat arbitrary, as in Eq. (S17) the square root operation, and it depends on which direction is considered a positive displacement of the phonon mode. Here, we would set $\mathcal{D}$ to follow the sign of phonon oscillation, that is, as indicated by the colored area in Fig. S7(b), the deformation potential is positive when $d(t)$ is also positive and vice versa.

Next we deal with the calculation of nonadiabatic coupling matrix element. The definition of deformation potential(Eq. (S16)), according to the chain rule, could be alternatively written as:

$$\mathcal{D} = \frac{1}{\dot{d}(t)} \langle Q(t)| \frac{\delta H(t)}{\delta t} |K(t)\rangle \tag{S18}$$

Make a time derivative on both side of the eigen equation satisfied by mode $\langle Q(t)|$, followed by an inner product with $|K(t)\rangle$, we then have:

$$\langle \dot{Q}(t)|K(t)\rangle = \frac{\langle Q(t)| \frac{\delta H(t)}{\delta t} |K(t)\rangle}{\epsilon_Q(t) - \epsilon_K(t)} \tag{S19}$$

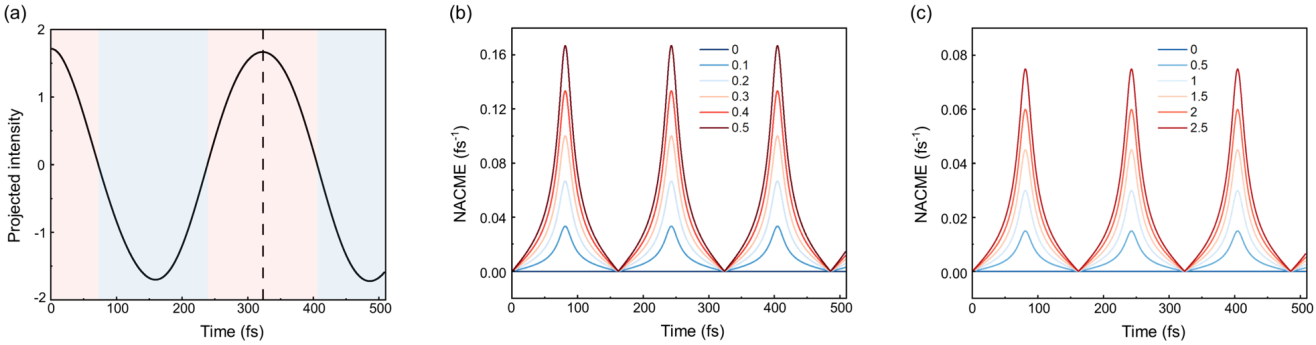

Figure S7. (a) Sign of deformation potential and phonon displacement. The area has been colored red when both the deformation potential and phonon displacement become positive and blue when negative. The dashed line indicate the time to calculate the absolute value of deformation potential. (b) Change of nonadiabatic coupling matrix element with respect to deformation potential $\mathcal{D}$. (c) Change of nonadiabatic coupling matrix element with respect to phonon amplitude of LA(M) mode.

Comparing Eq. (S18) and Eq. (S19), we finally obtain the analytical expression of the matrix element:

$$\langle \dot{Q}(t)|K(t)\rangle = \frac{\mathcal{D}\dot{d}(t)}{\epsilon_Q(t) - \epsilon_K(t)} \tag{S20}$$

In Fig. S7(b) and S7(c), we provide the variation of it to the deformation potential and the phonon amplitude of LA(M) mode. All the parameters involved in the model calculations have been listed in the following table:

TABLE II. Parameters for model calculation

ε_K (eV)	ε_K (eV)	$\mathcal{D}$ (eV/($\mathring{A}\cdot\sqrt{amu}$))	A ($\mathring{A}\cdot\sqrt{amu}$)	ω (THz)
1.91	1.81	0.154	1.72	3.09

S10. RESONANT EXCITATION OF A_1 MODE

To investigate the dynamical response of LA(M) mode under an effective time-dependent driving force from the A_1 mode, we first estimate an achievable A_1 mode amplitude by numerically solving its equation of motion under an external THz laser field, which is then used as input for our subsequent molecular dynamics simulations. For the infrared-active A_1 mode, it could couple

directly to the light field and the corresponding equation of motion could be written as [13, 14]:

$$\ddot{Q}_{A_1} + \omega_0^2 Q_{A_1} = \boldsymbol{Z^*} \cdot \boldsymbol{E_0} cos(\omega t) F(t), \tag{S21}$$

where $\boldsymbol{Z^*}$ is the mode effective charge vector and $\boldsymbol{E_0}$ is the peak electric field strength. $F(t) = \exp(-t^2/(2\tau^2))$ is the Gaussian shaped laser pulse, with a variance τ^2. While the A_1 mode of monolayer WSe_2 has a small mode effective charge estimated to be $|\boldsymbol{Z^*}|$=0.101 $e/\sqrt{amu}$, we note from Eq. S21 that additional constraint for the A_1 mode amplitude arises from the experimental capacities for strong terahertz pulse generation. From literature, high fields up to 100 MV/cm could be achieved in the low frequency regime (0.1-10 THz) using different techniques [15, 16]. To quantify the effect of the laser field, we carry out field-strength-dependent calculations with other laser field parameters, i.e., ω and τ, fixed to 7.55 THz in resonance with phonon frequency and 0.25 ps respectively. In Fig. S8(a) we show that amplitude of A_1 mode has a linear dependence on the THz field strength, where $Q_{A1} \sim 2.2$ Å$\cdot\sqrt{amu}$ (mean-squared amplitudes 0.01 Å^2, within the melting limit) can be realized with a strong THz field strength close to 65 MV/cm.

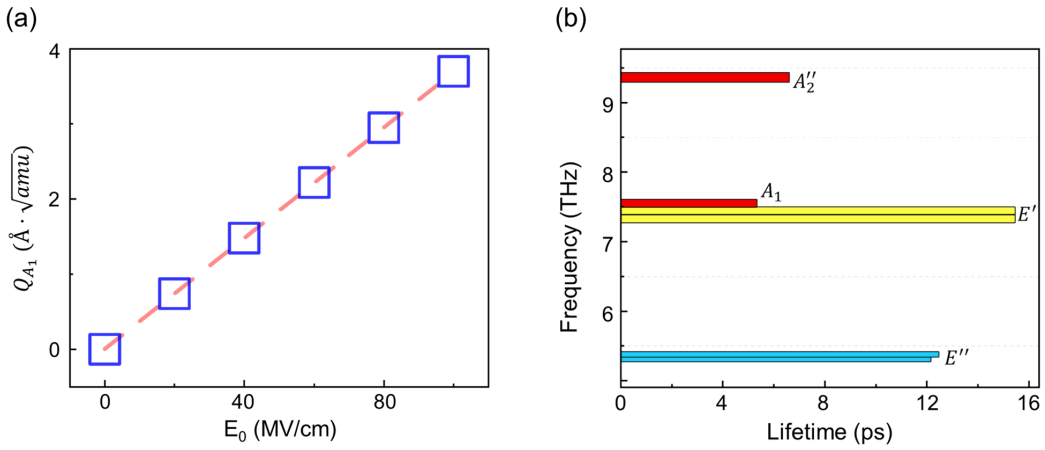

Figure S8. (a) Dependence of the resonantly excited A_1 mode amplitude Q_{A_1} on the peak field strength $\boldsymbol{E_0}$. (b) Phonon lifetime distribution at the Γ point near room temperature, with color representing the symmetry of each mode.

In our analysis above, we neglect the damping term of the coherent A_1 mode. This is also the case for our molecular dynamics simulations where the phonon motion has been accurately described in time domain yet at the cost of reduced scattering phase space compared with the statistical methods, for example, the real-time Boltzmann transport equations (rt-BTE) [17]. While

in practice the decay process is not negligible, the A_1 mode, based on the anharmonic phonon-phonon interactions, has a calculated lifetime of about 5 ps at room temperature (Fig. S8b), which is consistent with the one of 4.5 ps detected by time-resolved transmission measurements[18] and which could be longer at lower temperatures. Therefore, within the simulation time of ~ 1 ps where clear phonon down-conversion has been observed, one could assume the decay of the A_1 mode amplitude into other channels is negligible.

S11. NONLINEAR PHONONICS

We construct the lattice potential describing the nonlinear interaction up to the leading third order [19]:

$$V = \frac{1}{2}\Omega^2 Q_{A_1}^2 + \frac{1}{2}(\omega^2 + gQ_{A_1})Q_{LA}^2 \tag{S22}$$

where Ω, ω characterize the frequency of A_1 and LA(M) mode and g specifies the anharmonic coupling constant.

From the lattice potential, we write the equation of motion for LA(M) mode as:

$$\frac{\partial^2 Q_{LA}}{\partial t^2} + (\omega^2 + gQ_{A_1})Q_{LA} = 0 \tag{S23}$$

where Q_{A_1} oscillates coherently about the equilibrium position with normal mode frequency Ω and amplitude A' :

$$Q_{A_1} = A' cos(\Omega t) \tag{S24}$$

Under parametric resonance condition, we derive analytical solution for the equation as fitting function for the molecular dynamics result:

$$Q_M = ae^{st} cos(\omega + \frac{1}{2}\eta)t + be^{st} sin(\omega + \frac{1}{2}\eta)t \tag{S25}$$

where η is the frequency difference between the coupling mode $\eta = \Omega - 2\omega$. Besides, we have the fitting parameter s directly related to the anharmonic coupling constant g:

$$s^2 = \frac{1}{4}\left[(\frac{1}{2}\frac{gA'}{\omega})^2 - \eta^2\right] \tag{S26}$$

Fig. S9(a) shows the fitting result from which we obtain the coupling constant of 4.47 $meV/(\mathring{A} \cdot \sqrt{amu})^3$. The value keeps in well consistency with the one of 4.80 $meV/(\mathring{A} \cdot \sqrt{amu})^3$ extracted

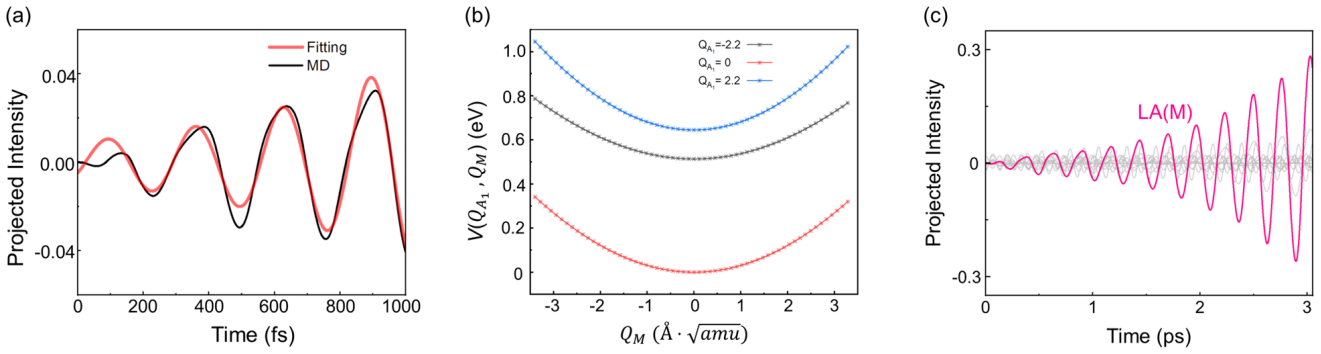

Figure S9. (a) Fitting curve(red) of the molecule dynamics simulation result(black). (b) Total energy as a function of the zone-boundary Q_{LA} coordinate for several values of the Q_{A_1} coordinate.(c) Atomic motion in a 3 ps molecular dynamics simulation projected onto the vibrational eigenmodes.

from polynomial fitting of the energy curve, see Fig. S9(b). The generation of LA(M) mode via its anharmonic interaction with A_1 mode is highly selective guaranteed by the exponentially growing amplitude. As is shown in Fig. S9(c), the LA(M) mode oscillates much more intensively than other modes within a timescale of 3 ps. Besides, from Eq. S26 we could provide several avenues towards the effective engineering of the LA(M) amplitude. For example, stronger LA(M) mode oscillation with an amplitude up to 1.7 Å·$\sqrt{amu}$, as large as the one used to drive electronic transition, could be obtained with an enhanced A_1 mode amplitude to 3.3 Å·$\sqrt{amu}$, which according to Fig. S8 could be excited under a ~90 MV/cm THz laser field. We do note that, although high fields up to 100 MV/cm could be achieved in practice, such high peak field might induce unwanted effects. Fortunately, it is proposed that the peak laser field required could be effectively reduced via the delicate design of optical cavities which can enhance the parametric resonance between the A_1 and LA(M) modes [20, 21]. Similar effect could also be obtained via the manipulation of the anharmonic phonon-phonon coupling constant g.

S12. REALIZATION OF THE STEP-LIKE SCATTERING

Previous experiments have reported the displacive excitation of an A_1 mode, which then decays coherently into the acoustic branches [19]. The displacive excitation of coherent phonons (DECP) can be well captured in our present TDDFT simulation. In Fig. S10 we show the dynamical response of A_1 mode after the resonant excitation of K valley electrons under a moderate laser field

(0.62 mJ/cm^2). This oscillatory lattice motion involves a shift of the equilibrium position, which corresponds to a modification of the interactomic lattice potential along the A_1 mode coordinate as in the DECP mechanism. The subsequent down-conversion of the A_1 mode into two acoustic branches could also be observed in our simulation (red curve in the figure).

The DECP mechanism provides another possible avenue towards the generation of LA(M) mode and the realization of the coherent-phonon-driven intervally scattering, where one laser pulse could disturb both the electron and lattice degrees of freedom. In theory, a large amplitude A_1 mode can be displacively excited under a strong laser field, although in practice these carrier-based mechanisms suffer from the ultrafast heating effects which could induce severe decoherence effect and limit the coherent phonon amplitudes [22]. Therefore, the advances of THz lasers provide better opportunities to resonantly excite A_1 mode with large amplitude and then drive the LA(M) mode as discussed for nonlinear phononics.

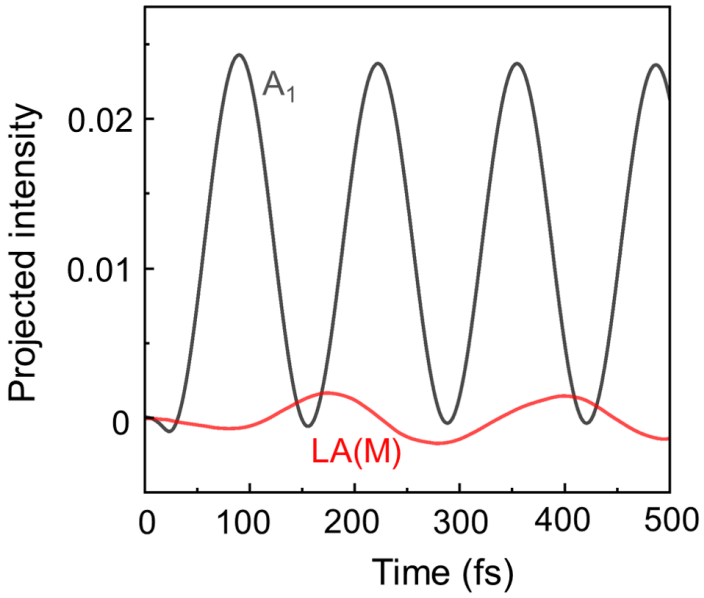

Figure S10. Displacive excitation of A_1 mode (grey) and subsequent phonon down-conversions into the LA(M) mode (red).

Different from the carrier-based mechanism, the THz pulse for the resonant excitation of coherent phonons could hardly disturb the electron subsystem due to the energy mismatch. In our simulations, we create an ideal condition where the coherent lattice oscillation along LA(M) mode can be driven prior to the electronic excitation. In practice, this can possibly be realized by a two-pulse process with the first THz field coupling to the infrared (IR) active phonon mode and inducing subsequent phonon down-conversions, followed by the second pulse with much higher energy to excite the K valley electrons. Meanwhile, we hope to motivate future experimental exploration to test the limit of our predicted coherent-phonon-driven phenomena.

[1] E. Runge and E. K. U. Gross, Phys. Rev. Lett. **52**, 997 (1984).

[2] J. C. Tully, Faraday Discuss. **110**, 407 (1998).

[3] S. Meng and E. Kaxiras, J. Chem. Phys. **129**, 054110 (2008).

[4] C. Lian, M. Guan, S. Hu, J. Zhang, and S. Meng, Adv. Theory. Simul. **1**, 1800055 (2018).

[5] C. Lian, S.-J. Zhang, S.-Q. Hu, M.-X. Guan, and S. Meng, Nat. Commun. **11**, 43 (2020).

[6] H.-Y. Chen, D. Sangalli, and M. Bernardi, Phys. Rev. Res. **4**, 043203 (2022).

[7] G. Onida, L. Reining, and A. Rubio, Rev. Mod. Phys. **74**, 601 (2002).

[8] J. Sun, C.-W. Lee, A. Kononov, A. Schleife, and C. A. Ullrich, Phys. Rev. Lett. **127**, 077401 (2021).

[9] K.-Q. Lin, C. S. Ong, S. Bange, P. E. Faria Junior, B. Peng, J. D. Ziegler, J. Zipfel, C. Bäuml, N. Paradiso, K. Watanabe, T. Taniguchi, C. Strunk, B. Monserrat, J. Fabian, A. Chernikov, D. Y. Qiu, S. G. Louie, and J. M. Lupton, Nat. Commun. **12**, 5500 (2021).

[10] R. MacKenzie, E. Marcotte, and H. Paquette, Phys. Rev. A **73**, 042104 (2006).

[11] M. Lazzeri, C. Attaccalite, L. Wirtz, and F. Mauri, Phys. Rev. B **78**, 081406 (2008).

[12] M. Hellgren, J. Baima, R. Bianco, M. Calandra, F. Mauri, and L. Wirtz, Phys. Rev. Lett. **119**, 176401 (2017).

[13] D. M. Juraschek and S. F. Maehrlein, Phys. Rev. B **97**, 174302 (2018).

[14] D. M. Juraschek, Q. N. Meier, and P. Narang, Phys. Rev. Lett. **124**, 117401 (2020).

[15] J. A. Fülöp, S. Tzortzakis, and T. Kampfrath, Adv. Opt. Mater. **8**, 1900681 (2020).

[16] A. D. Koulouklidis, C. Gollner, V. Shumakova, V. Y. Fedorov, A. Pugžlys, A. Baltuška, and S. Tzortzakis, Nat. Commun. **11**, 292 (2020).

[17] X. Tong and M. Bernardi, Phys. Rev. Res. **3**, 023072 (2021).

[18] T. Y. Jeong, B. M. Jin, S. H. Rhim, L. Debbichi, J. Park, Y. D. Jang, H. R. Lee, D.-H. Chae, D. Lee, Y.-H. Kim, S. Jung, and K. J. Yee, ACS Nano **10**, 5560 (2016).

[19] S. W. Teitelbaum, T. Henighan, Y. Huang, H. Liu, M. P. Jiang, D. Zhu, M. Chollet, T. Sato, É. D. Murray, S. Fahy, *et al.*, Phys. Rev. Lett. **121**, 125901 (2018).

[20] D. M. Juraschek, T. c. v. Neuman, J. Flick, and P. Narang, Phys. Rev. Res. **3**, L032046 (2021).

[21] J. B. Curtis, M. H. Michael, and E. Demler, (2023), 10.48550/ARXIV.2301.01884.

[22] H. Padmanabhan, M. Poore, P. K. Kim, N. Z. Koocher, V. A. Stoica, D. Puggioni, H. (Hugo) Wang, X. Shen, A. H. Reid, M. Gu, M. Wetherington, S. H. Lee, R. D. Schaller, Z. Mao, A. M. Lindenberg, X. Wang, J. M. Rondinelli, R. D. Averitt, and V. Gopalan, Nat. Commun. **13**, 1929 (2022).